RSC Advances

ROYAL SOCIETY OF CHEMISTRY

www.rsc.org/advances

Support information

Observing wetting behaviors of UV-curable liquid on nanostructured surfaces with sub-20nm resolution

Jie Bian, ‡ Xinxin Fu, ‡ Jing Hu, ‡ Yushuang Cui, ‡ Zhiwei Li, ‡ Changsheng Yuan, *, ‡ Haixiong Ge, Wen-Di Li, *, † Yanfeng Chen‡

‡Department of Materials Science and Engineering, College of Engineering and Applied Sciences, National Laboratory of Solid State Microstructures, Nanjing University,

Nanjing, 210093 (P. R. China)

† Department of Mechanical Engineering, University of Hong Kong, Pokfulam, Hong Kong, P. R. C.

***Corresponding Author:** E-mail: csyuan@nju.edu.cn; liwd@hku.hk

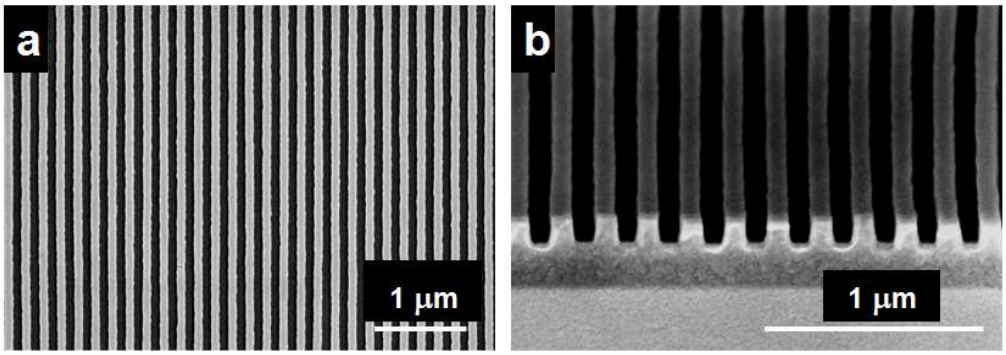

Figure S1. SEM images of the as-imprinted 200 nm pitch nanogrooves: (a) top view and (b) cross-sectional view.

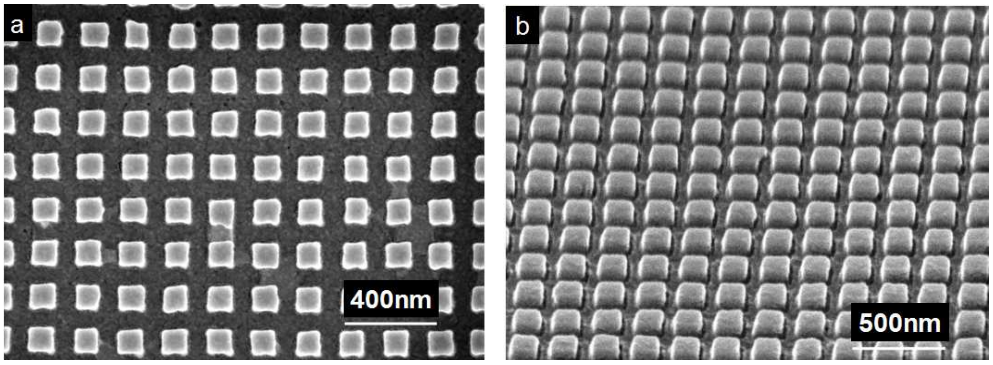

Figure S2. SEM images of the 200 nm pitch nanopost arrays: (a) top view and (b) tilted view.

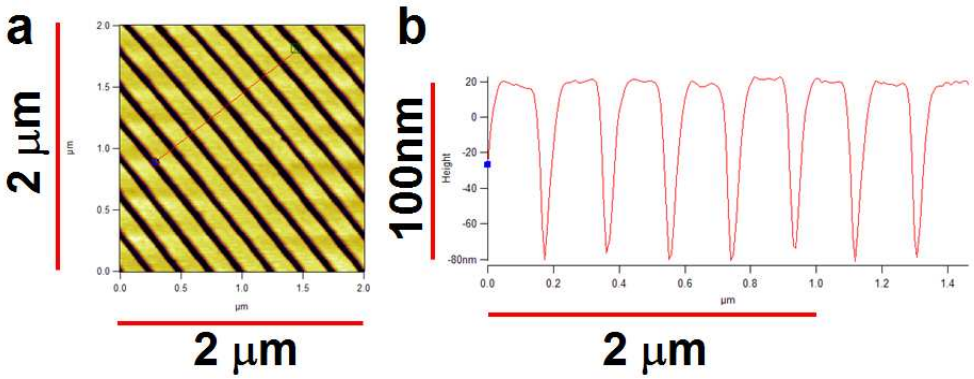

Figure S3. AFM images of the 200 nm pitch nanogrooves after silanization: (a) plane-view image; (b) line cut profile of the corresponding image in (a).

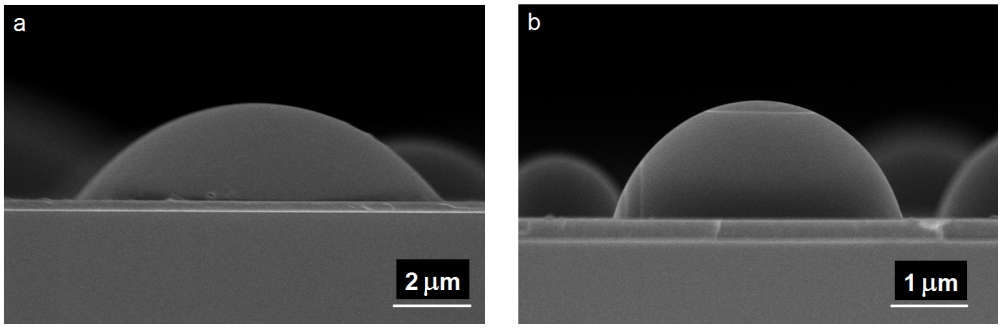

Figure S4. SEM images of cross-section of solidified microdroplets on smooth surface coated by self-assembled monolayers (SAMs) of trichlorofluoroalkylsilane: (a) HH liquid and (b) LH liquid

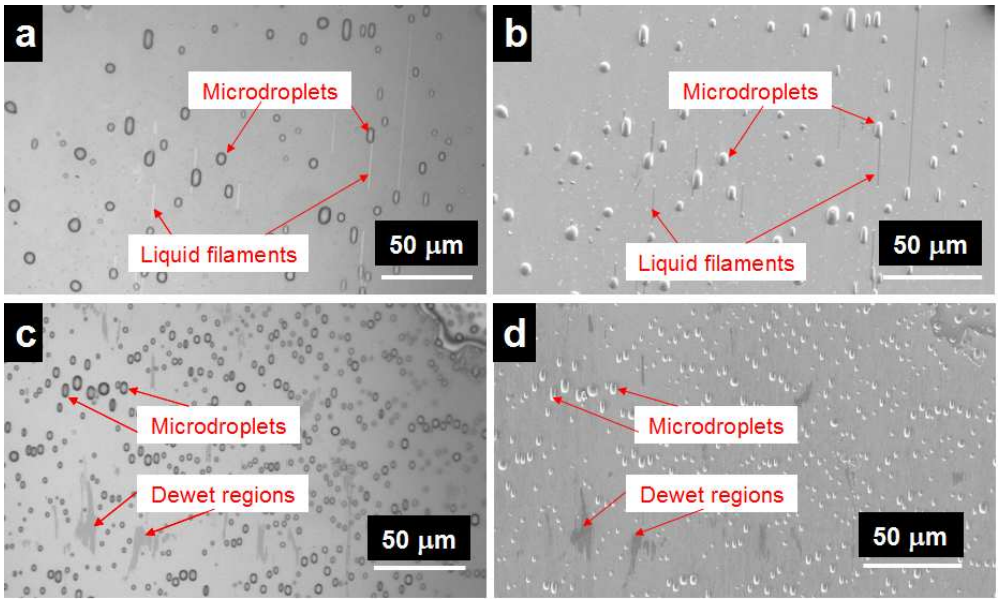

Figure S5. Microscopic images of microdroplets before crosslinking (a) HH liquid and (c) LH liquid and SEM images of the droplets at corresponding same positions after crosslinking (b) HH liquid and (d) LH liquid.

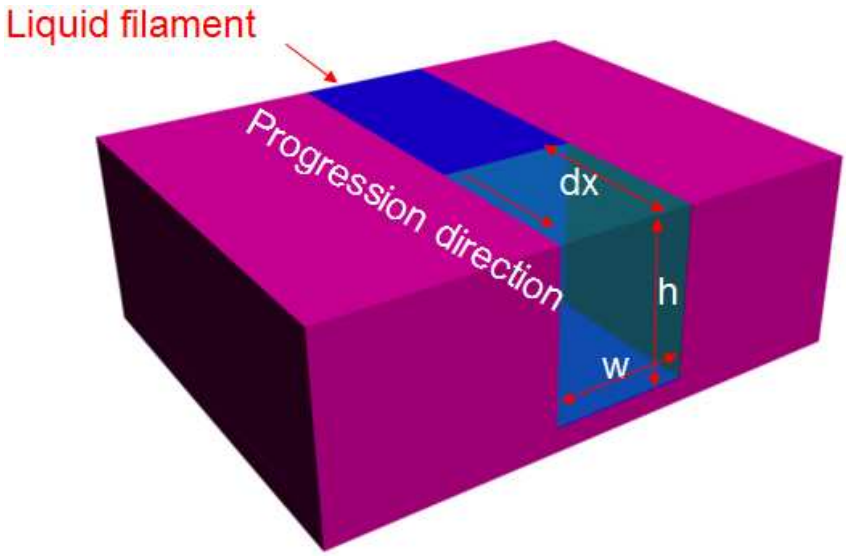

Figure S6. Schematic of progression of liquid (in blue) in a rectangular nanogroove.

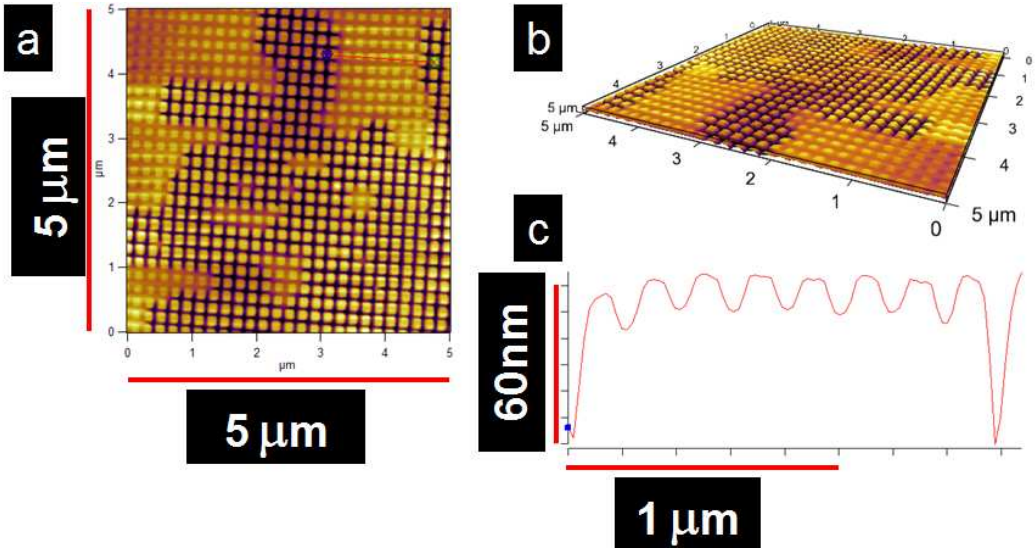

Figure S7. AFM images of solidified HH liquid on 200 nm pitch nanopost arrays coated by trichlorofluoroalkylsilane : (a) plane-view AFM image; (b) three-dimensional AFM perspective view of (a); and (c) line cut profile of the corresponding image in (a).

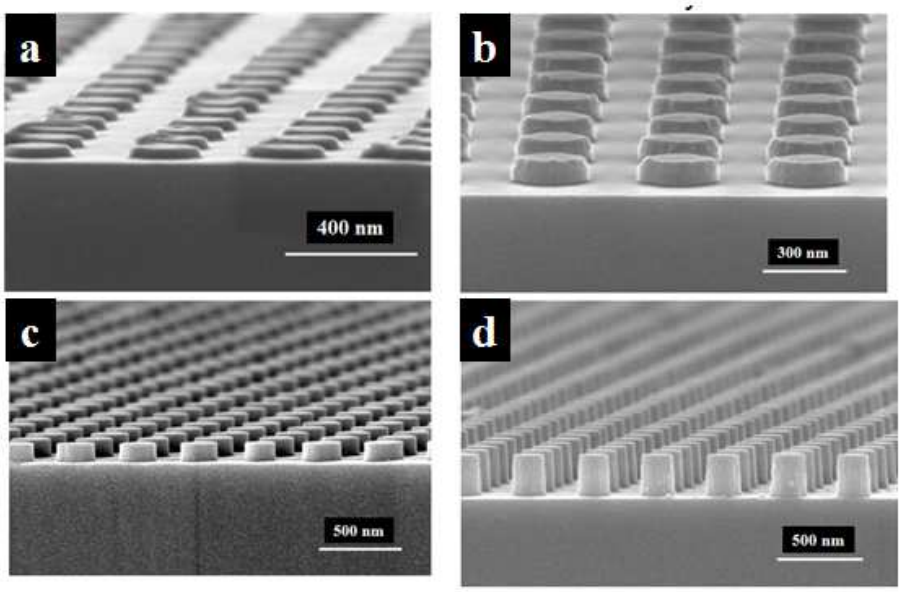

Figure S8. SEM images of the 400 nm pitch cylindrical nanopost arrays with different post heights of (a) 35nm, (b) 65nm, (c) 110nm height, and (d) 250nm.

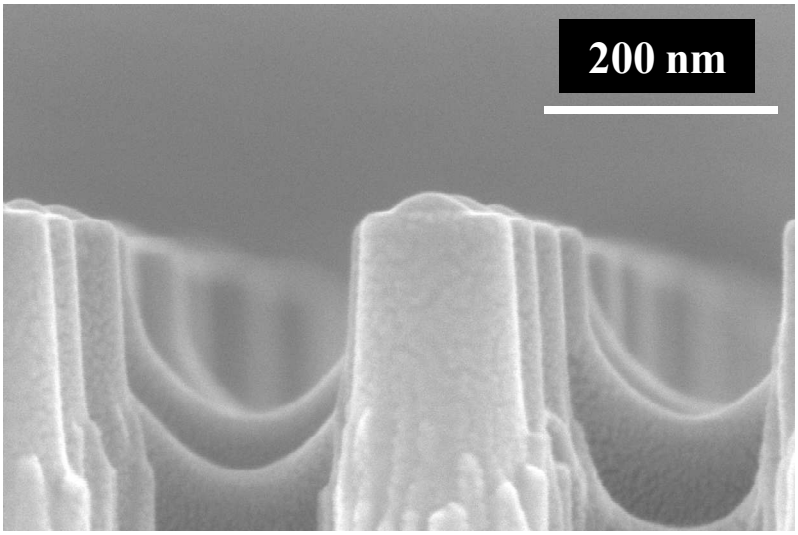

Figure S9. SEM image of the cross-sectional view of solidified liquid on the 400 nm pitch cylindrical nanopost array, with the nanodroplets visible on the top of the nanoposts and the menisci between the nanoposts.

Cite this: DOI: 10.1039/c0xx00000x

www.rsc.org/xxxxxx

ARTICLE TYPE

Observing wetting behaviors of UV-curable liquid on nanostructured surfaces with sub-20nm resolution

Jie Bian,[a] Xinxin Fu,[a] Jing Hu,[a] Yushuang Cui,[a] Zhiwei Li,[a] Changsheng Yuan,*[a] Haixiong Ge, *[a] Wen-Di Li*[b] and Yanfeng Chen*[a]

Received (in XXX, XXX) Xth XXXXXXXXX 20XX, Accepted Xth XXXXXXXXX 20XX
DOI: 10.1039/b000000x

In this work, the liquid acrylated materials were transferred onto the nanostructured surfaces by a transfer printing method. Further, they were frozen (solidified) by UV-light exposure. The morphology of the solidified liquid reflects the original liquid-state profile because the UV-curing shrinkage of the acrylated material was only a few percent in volume so that it would not largely alter the liquid morphology. The cured samples were then examined with high resolution SEM or AFM measurement. This proposed method allows for the observation of liquid behavior down to sub-20nm scale with more subtle details such as nano-menisci between nanogrooves, and liquid bridges covering nanostructures. The wetting behavior of the liquid strongly depends on the surface properties and geometries of the underlying nanostructures. Experimental results agree with the prediction of a simple surface energy variation model. They indicate that macroscopic wetting behaviors of liquid are preserved as dimensions go down to 100 nm.

Introduction

The wetting behaviors of liquids on nanostructures have received continuous attention from fundamental sciences and applied technologies, including surface science[1-4], microfluidics[5,6], hydrodynamics[7,8], biomimetics[9-11], surface coating[12,13], anti-fogging[14] and fog-harvesting[15,16], inkjet printing[17,18], biotechnology[19,20] and thin-film lubrication [21,22]. To better understand the wetting behaviors of the nanostructures, it is essential to look at the subtle features of the wetting morphologies with a close inspection at a local scale. The investigation of the interaction of the liquid with nanostructures at this scale is an emerging research area. It is still in its infancy stage and suffers from the lack of high spatial resolution observation techniques. Currently, Atomic force microscopy (AFM) [23-25], and environmental scanning electron microscopy (ESEM) [26-28] are the most widely used techniques for observing liquid on nanostructured surfaces. Despite the recent progress in the named methods, many challenges still remain for both techniques. AFM has the capability of observing liquid morphologies down to nanoscale dimension and operate in ambient environment (air). However, the interaction between the AFM tip and the liquid can change the measured liquid profile and give rise to artifacts in the obtained image. Additionally, the time consuming AFM measurement limits its application for imaging volatile liquid, because the liquid morphology may vary in different ways during evaporation. On the other hand, the ESEM (or low-vacuum SEM) permits imaging of hydrated nonconductive samples and has been successfully applied to overcome the evaporation problem, but its resolution rests in micrometer range and is still much lower than that on metal-coated samples. However, neither of these two methods can exhibit the real cross-section of the liquid filling into the nanostructure. Up to now, few existing methods can provide a direct observation for the interplay between liquid and structures down to nanometer scale.

Seemann et al. [29] created liquid structures on micro-grooved surface by vapor condensation of the polystyrene. The structures of the liquefied polymer were solidified by lowering the temperature below the glass transition temperature of the polystyrene, and were then scanned by atomic force microscopy (AFM) without the aforementioned disadvantages. Krupenkin et al.[30] dispensed UV polymerizable liquid droplets on nanostructures and solidified them by UV irradiation, then investigated their morphologies using SEM. Kusumaatmaja et al. [31] created liquid monomer droplets on sub-micrometer-scale corrugated surfaces by microtransfer printing. The subsequent polymerization preserved the geometry of the liquid drop and enabled analysis afterward. Here, we present a combination of methods mentioned above, to record subtle features of liquid morphologies with sub-50 nm resolution based on the UV-curable resins (solidifying liquid) on nanostructures. The wetting morphologies of the UV-curable liquid were created on nanostructures by a transfer printing method. These morphologies were instantaneously solidified by the exposure of UV-light, and then were characterized by high resolution SEM or AFM measurement. The image of solidified liquid is a good indication of the liquid state, because the UV-curing shrinkage of the acrylated materials was only 6~7 percent in volume[32] so that it

would not largely change the original liquid morphology.

Experimental

Materials

A high hydrophobic (HH) acrylated monomer (acrylated siloxane) and, trichloro (1H,1H,2H,2H-perfluorooctyl) silane were purchased from Gelest. A low hydrophobic (LH) acrylated monomer (a hexafunctional urethane acrylate) was kindly provided by Sartomer. The photo initiator, Irgacure 184, was obtained from Ciba. Also, homemade silicon containing multifunctional acrylate composition was used as the UV-curable nanoimprint resist.

Fabrication of nanostructured surfaces

The nanostructured surfaces were fabricated by UV-curing nanoimprint lithography. The UV-curable nanoimprint resist was spin-coated onto the silicon wafer at 2000 rpm for 40s to get a 270nm thickness smooth film and was imprinted by an imprint machine with combined thermal- and UV imprint capabilities from ImprintNano, China. The surfaces of imprinted nanostructures were modified with a brief treatment of O_2 plasma (30W power, 5sccm oxygen flow for 1 min) and then coated with a self-assembled monolayer of trichloro(1H, 1H, 2H, 2H-perfluorooctyl)silane by vapor phase deposition in a closed dry container for 24 h.

Transferring and solidifying UV-curable liquid on nanostructured surfaces

Both processes of transferring and solidifying UV-curable liquid on nanostructure surfaces are summarized in Figure 1. Initially, the UV-curable liquid is spin-coated onto a silicon wafer at 2000 rpm for 40s to form a 270nm thick film (Figure 1a). Next, a blank hybrid mold with a smooth surface is placed on the spin-coated UV-curable resist (Figure 1b). After separation from the silicon wafer (Figure 1c), the mold is placed on the nanostructure surface (Figure 1d).The mold will spontaneously stick to the nanostructure surface by liquid capillary force without additional pressure.After the mold is removed from the nanostructure's surface (Figure 1e), the UV-curable liquid remains on the surface and is then cured by the UV-light exposure (Figure 1f).

Measurement

SEM images were taken with a HITACHI S-4800 and a Carl Zeiss Supra 55 field-emission scanning electron microscope at 3.0 kV. AFM measurements were taken with a NT-MDT NSG20 in tapping mode. Contact angles were measured on a Dataphysics OCA30 CA system at ambient temperature.

Results and discussion

Acrylate-based resins have been widely used in various UV-curable material systems as the backbone due to their great reactivity with a wide choice of acrylated monomers. Hence, by directly selecting or mixing a range of acrylate-based materials, one can formulate a UV-curable material with the desirable properties. In this work, two different acrylated resins; a high hydrophobic (HH) monomer (acrylated siloxane with a viscosity of 110 cps and contact angle (θ) of 58.8±1.3° on a smooth hydrophobic surface formed by self-assembled monolayers (SAMs) of trichloro (1H,1H,2H,2H-perfluorooctyl) silane), and a low hydrophobic (LH) monomer (a hexafunctional urethane acrylate with a viscosity of 1600 cps and contact angle of 85.6±1.8° on a smooth hydrophobic surface) were employed as the UV-curable liquids. Aside from the acrylated monomer, the UV-curable liquid consisted of 1.0 wt% photoinitiator (Irgacure 184) to the monomer and reactive diluent methyl acrylate for spin coating. Two different nanostructures were fabricated by employing UV-curing nanoimprint lithography and acrylated siloxane material[33]. Figure S1 of the support information depicts grooves with 200 nm pitch and 140 nm depth, Figure S2 of the support information depicts square posts with 200 nm pitch and 110 nm height. In order to make the surface of the nanostructures hydrophobic, the surface was treated with SAMs of trichlorofluoroalkylsilane. Figure S3 show that the silanization hardly changed the morphology of 200 nm pitch nanogrooves, and the RMS roughness on the ridge of nanogrooves is 2.0±0.5nm.To investigate the wetting behavior on nanostructures at micro and nanoscale, the bulk liquid must be transferred onto the nanostructured surface. In this work, the UV-curable liquid was formed on the nanostructured surface by a transfer printing method. The process of the transfer printing is illustrated in Figure 1. A blank hybrid nanoimprint soft lithography mold[34,35]consists of a smooth crosslinked polymer film on an elastic poly (dimethylsiloxane) (PDMS) was employed as a carrier medium. First, a thin and uniform film of UV-curable liquid (resist) was spin-coated on a silicon wafer. Then, the mold was placed on the resist, covering the silicon wafer from one edge to the other edge. After a conformal contact between the mold and the silicon wafer, the mold was detached from the silicon wafer and part of the UV-curable liquid was adhered to the mold. The adhered liquid would ball up into droplets on the smooth surface of the blank mold by the minimization of surface energy. The mold was subsequently placed against the nanostructured surface. During this stage, the adhered liquid droplets were sandwiched between the blank mold and the substrate and would be not only pressed into the nanostructures but also planarized to extend into close contact with nearby droplets and merge into an integrated liquid film on the substrate [35]. The UV-curable liquid was partially transferred onto the nanostructured surface after the mold was removed. The liquid would simultaneously turn to the thermodynamic equilibrium or metastable wetting morphologies. Finally, the UV-curable liquid on the nanostructures was instantaneously solidified by the exposure to the UV-light. Afterward, the solidified liquid is characterized by SEM and AFM.

Figure 5S shows the microscopic images of the uncured wetting morphologies and SEM images of the morphologies after photocrosslinking in oxygen free environment for HH and LH liquids.The various wetting morphologies, including microdroplets, liquid filaments and dewet regions, have almost no change in UV curing process both for HH and LH liquid, hence the cured morphologies can be used to research the wetting behaviors for both liquids before crosslinking in this paper.

SEM images of the HH and LH UV-curable liquid droplets on the hydrophobic nanogrooves after curing are shown in the left and right columns of Figure 2. The SEM images at low

magnification show that the wetting behaviors of HH and LH liquid are significantly different. HH liquid resist droplets exhibit a consistent appearance over the sample surface, aside from some elongated micro-droplets randomly distributed on the surface, and a few dark filaments connecting the micro-droplets However, the LH resist exhibited a bright-and-dark marbleized surface, scattered with elongated micro-droplets. The insets of Figure 3a and b are the contact angle measurement of HH and LH liquid on the smooth hydrophobic surface, respectively. The HH liquid was more lyophilic (exhibit more wettability) than the LH liquid on the hydrophobic surface, therefore the HH liquid shown a smaller contact angle. From the SEM images with higher magnification we could distinguish the differences between the wetting behaviors of the HH and LH liquid on the nanogrooves. Various wetting morphologies coexisted on the nanostructures for both liquids. In Figure 2d it was observed that the dark regions represent the nanogrooves filled with the liquid and the bright regions represent the empty nanogrooves with no liquid. Menisci of the liquid filled in the nanogrooves, formed the boundary of the dark and bright regions in Figure 2h. The micro-droplets were elongated along the groove direction and only resided on the dark region (Figure 2d). As for the HH liquid, it was absorbed into the entire length of the grooves therefore, the SEM image showed a uniform contrast across the nanogroove surface, because there is only a slight variation in the projected height between the groove ridges and liquid-filled channels (Figure 2c). The dark filaments were liquid bridges, which extended from micro-droplets and covered several ridges of the nanogrooves (Figure 2e). If the images were continually zoomed in, more subtle features of the wetting morphologies could be observed. It was found that chains of isolated nanodroplets were located on top of the groove ridges for both liquids in Figure 2f and g. These isolated nanodroplets also indicate that the liquid film did not cover the top of the ridge. The shapes of the nanodroplets were strongly influenced by the droplet size. If the contact diameter of the droplet was larger than the width of the groove ridge, the droplet was elongated along the ridge to exhibit an oval shape. Otherwise, if the contact diameter was less than the width of the ridge, then the droplet approached a spherical cap (Figure 2h). It was also observed that the nanodroplet could adhere to the sidewall of the groove (Figure 2g). In right image of Figure 2g, the smallest droplet that could be seen on the nanogrooves was 20 nm in diameter. There is a possibility for existence of much smaller droplets on the groove surface; however it was difficult to distinguish them from the roughness of the surface (2.0±0.5nm RMS in supporting information).

To achieve a better understanding of liquid behavior on nanogrooves, the samples were carefully broken, and the cross section of wetting morphologies of the solidified liquid were captured by SEM. Figure 3 shows the SEM images of the HH and LH liquid resists, respectively. The two liquids also showed different filling behaviors. For HH liquid, the liquid filled all the channels, and some liquid bridges covered several ridges of the nanogrooves (Figure 3a and c). However, for LH liquid, only parts of the channels were filled and the others were empty (Figure 3b and d). Liquid filled areas correspond to the dark and empty areas correspond to the bright regions on the top view of the SEM image (Figure 2b). AFM measuring was done to confirm the SEM observations (Figure 4a and b). The AFM results were in agreement with the SEM images. Series of isolated nanodroplets were found on top of the groove ridges (Figure 4b), additionally, parts of the channels were filled with the liquid and others were empty (Figure 3a). AFM produces deformed shapes when the size of the measured object is comparable to that of the AFM tip, thus the AFM image of the cross-sectional profile for the rectangular groove, displayed a V-shape bottom (Figure 4c).

When the blank mold is inked with the UV-curable liquid from the spin-coated film, it is placed on the nanogrooves. The liquid resist would fill in the grooves and after removal of the mold, part of the liquid would remain on the nanogrooves. However, the remaining liquid resist would now become a non-equilibrium state. The interfacial free energies between the solid, the liquid, the vapor and the topography of the nanostructures would drive the liquid toward equilibrium or metastable state. Quéré et al.[36] systematically studied the wetting properties of liquids on micro and nanostructured surfaces. The complete wetting of any surface is only achieved when the $\theta = 0$. This means that it is impossible to induce a wetting transition by texturing a solid. Due to the fact that the contact angles of both UV-curable liquids are larger than 0, both liquids formed droplets on top surface of the nanogrooves. Since the top of the ridges was uncovered by the liquid film, the liquid behavior in the nanogroove array could be studied using a simplified model which considers liquid in a single isolated nanogroove. As the liquid progresses in a rectangular groove (Figure S6) with a width w, and a depth h, the surface energy variation dE arising from an apparent displacement dx of the liquid can be described as

$$dE = (\gamma_{SL} - \gamma_{SA})(2h + w)dx + \gamma w dx$$

where γ_{SA}, γ_{SL} and γ are the solid-air, solid-liquid and liquid-air interfacial tensions, respectively. The first term in Equation 1 is related to the replacement of an empty groove by a liquid one. It is proportional to the groove area, i.e. (2h + w). The second term is related to the creation of a liquid/vapor interface associated with the film progression. Using the Young equation, $\gamma_{SA}-\gamma_{SL} = \gamma\cos\theta$, where θ is the contact angle of the liquid on an ideal flat surface with the same chemical composition as the groove, we have

$$dE = -\gamma\cos\theta(2h + w)dx + \gamma w dx$$

For dE=0, the critical contact angle θc, for the favorable liquid progression can be expressed as

$$\cos\theta_c = \frac{w}{2h + w}$$

The liquid progression is favorable (dE < 0) in the groove provided that the liquid contact angle, θ, is smaller than θc. In this case, the width and depth of the nanogrooves were around 100nm and 140nm, respectively, which were determined by the nanoimprinted mold and measured with SEM. The θc of the nanogroove was calculated to be 74.7°. The contact angles of the HH and LH liquid on the flat surface coated with trichlorofluoroalkylsilane were 58.8±1.3° (<θc) and 85.6±1.8° (>θc), respectively. The SEM observation was in agreement with the predicted results. The HH liquid filled the full length of the

nanogroove while the LH liquid partially receded from the groove. Besides the thermodynamic equilibrium states, metastable states were also achieved, HH liquid bridges spanned several ridges of the nanogrooves because the sharp edges of the ridges represented energy barriers for the retracting of the liquid film and locally pinned the filament to the upper edges of the grooves.

Similar experiments were done on a surface decorated with square nanoposts. Figure 5a and b show the wetting behaviors of HH and LH liquid on the nanoposts coated with trichlorofluoroalkylsilane, respectively. The liquid film should also recede to ball up on the flat top of the nanoposts because their contact angles were much larger than 0. Their wetting properties could still be interpreted by Quéré's model [37] written as

$$dE = (\gamma_{SL} - \gamma_{SA})(r - \varphi_S)dx + \gamma(1 - \varphi_S)dx$$

Where the r is the solid roughness of the nanoposts surface (ratio of the actual solid area over its projected one) and φ_S is the nanoposts density. The replacement of an empty trench of the nanoposts by a liquid was proportional to $r - \varphi_S$, whereas the liquid/vapor interface increased in the trench and was proportional to $1 - \varphi_S$. Therefore, the critical contact angle θc, for the favorable liquid progression in the nanoposts could be expressed as

$$\cos\theta_c = \frac{1 - \varphi_S}{r - \varphi_S}$$

For the square nanoposts with the size of 110 nm, pitch of 200 nm and height of 110 nm, we obtained r = 2.2 and φ_S = 30%. Its θc was calculated to be 68.4°. Since the contact angle of the LH liquid was larger than 68.4°, the liquid exhibited a dewetting property on the nanoposts surface. It receded through the trenches of the nanoposts and balled up to micro-droplets (Figure 5b). The shape of the micro-droplets was deformed by the pinning effect of the nanoposts and partially conformed to the nanoposts array (Figure 5d). In addition, the liquid film left on top of the isolated nanopost also balled up to a nanodroplet (Figure 5d). HH liquid showed a wetting property on the nanoposts. Almost all trenches of the nanopost were filled by the liquid because its contact angle was smaller than 68.4°. Unlike the LH liquid, which balled up to a nanodroplet, the HH liquid spread out on the top facet of the nanopost. This might be attributed to very small surface area of the top of a single nanopost and stronger pining effect at the four edges of the nanopost compared to the LH liquid, which locally hindered the liquid film from receding to nanodroplets. It was observed that local dewetting (nanogaps) happened at several parts of the nanoposts surface, which might be caused by the defects of the SAM coating of trichlorofluoroalkylsilane (Figure 5a and c).

A series of square arrays of cylindrical silicon nanoposts with various aspect ratios (ratio of the post height to the pitch) were fabricated by nanoimprint lithography and reactive ion etching, and then coated with a SAM layer of trichlorofluoroalkylsilane (Figure S8). Post diameter d and pitch p were almost fixed (about 200 and 400 nm, respectively) from the imprint mold, while the height h was varied by the etching time of RIE. In the case of cylindrical posts, we had $r = 1 + \pi dh/p2$ and $\varphi_S = \pi d2/4p2$. Figure 6 shows the wetting behaviors of the HH liquid on the square arrays of cylindrical silicon nanoposts with various aspect ratios. For a small aspect ratio post, it was observed in Figure 8a that almost all the liquid was drained from the cavities between the nanoposts and balled up to micro-droplets. As the aspect ratio increased, the liquid morphologies gradually transited from a drainage state to an imbibitional state (Figure 6b, 6c). This is because the critical contact angle increased with the increase of the post aspect ratio. Once the contact angle of the liquid was less than the critical contact angle, dE would become less than zero, which would drive the liquid imbibed into cavities between the nanoposts. If the volume of the liquid was smaller than that of the cavities, the liquid could not completely wet all the cavities, while it would also assemble in the cavities, just as the liquid film balling up droplets on the flat surface due to its contact angle > 0 (Figure 6d). More subtle details of the liquid behaviors could be obtained from the observation of the cross-section of the nanoposts arrays (Figure 6e, 6f). The liquid film would conform the shape of the textures in incompletely imbibitional state on 110 nm depth nanoposts surface (Figure 6e) and the meniscus at the centre of liquid film was higher than the one at the edge for 250nm depth nanoposts (Figure 6f). The liquid remained on top of the circle nanopost, balled up to nanodroplet (Figure 6f) and the contact angle was approximately the same as that of its macroscopic droplet (Figure S9). The observation was in a good agreement with the prediction of a simple surface energy variation model.

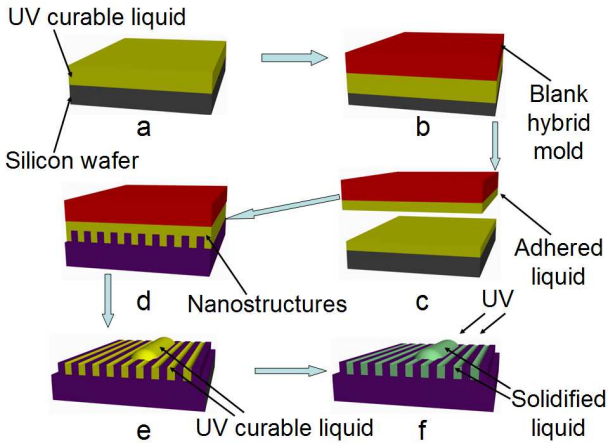

Fig 1. Schematic of transferring and solidifying UV-curable liquid on nanostructured surface: (a) spin-coating UV-curable liquid on silicon wafer; (b) placing blank hybrid mold on the spin-coated liquid; (c) separating the mold from the wafer; (d) placing the mold on nanostructured surface; (e) removing the mold from nanostructured surface; (f) solidifying the liquid by UV-light exposure.

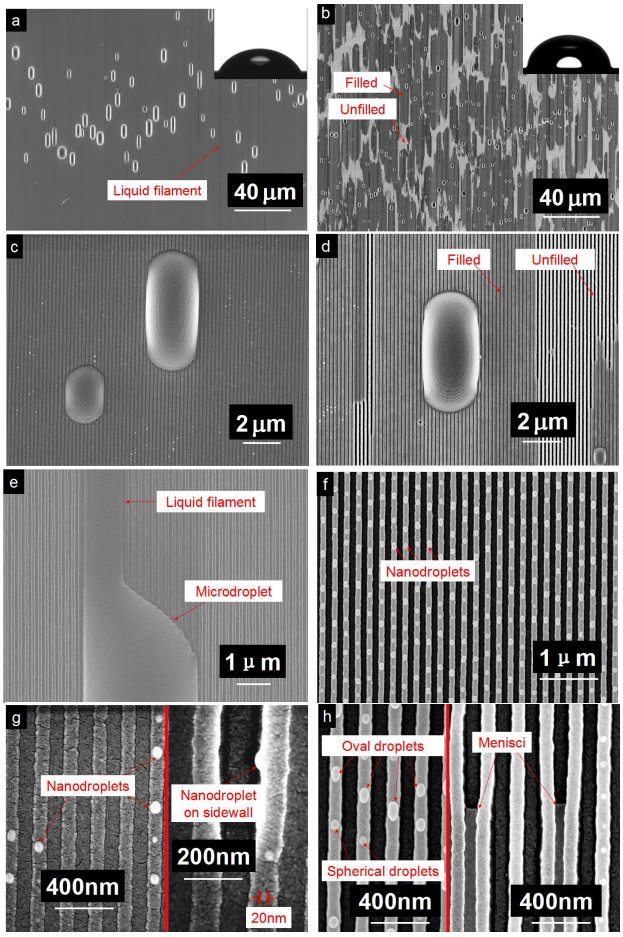

Fig 2. Top view SEM images of the solidified HH and LH liquid on hydrophobic naonogrooves (a) HH liquid with low magnification, the inset is the contact angle of HH liquid on the flat surface with the same surface chemical properties as nanogrooves; (b) LH liquid with low magnification and the inset is contact angle of LH liquid on the same flat surface; (c) zoomed-in image of (a); (d) zoomed-in image of (b); (e) liquid filament extended from a microdroplet; (f) chains of isolated nanodroplets on the roofs of the nanogrooves; (g) higher magnification images of HH liquid (h) higher magnification images of LH liquid.

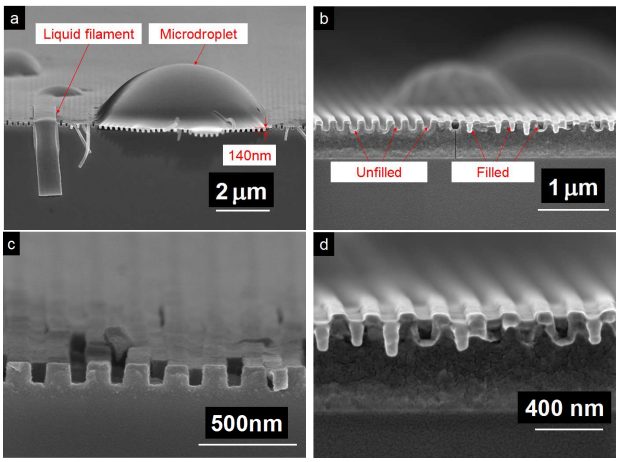

Fig 3. Cross-sectional SEM images of solidified HH and LH liquid on hydrophobic naonogrooves: (a) HH liquid with low magnification; (b) LH liquid with low magnification; (c) zoomed-in image of HH liquid; and (d) zoomed-in image of LH liquid.

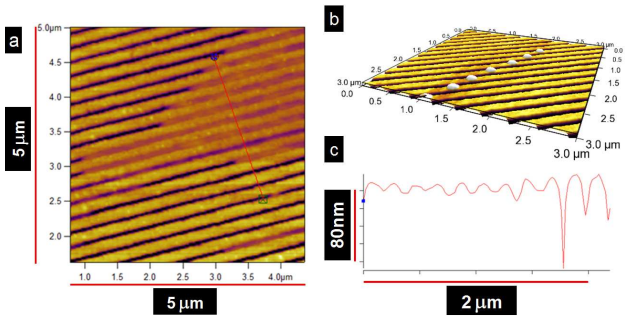

Fig 4. AFM images of solidified LH liquid on hydrophobic naonogrooves: (a) Plane-view AFM image; (b) three-dimensional AFM perspective view of isolated nanodroplets on the roofs of the nanogrooves; and (c) line cut profile of the corresponding image in (a).

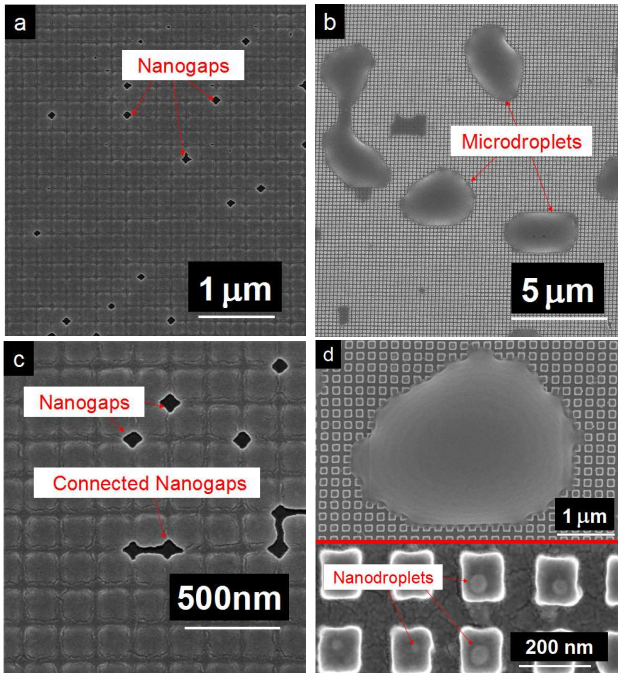

Figure 5. Top view SEM images of the solidified HH and LH liquid on 200nm pitch square nanopost arrays with hydrophobic surface: (a) HH liquid with low magnification; (b) LH liquid with low magnification; (c) zoomed-in image of (a); and zoomed-in images of (b).

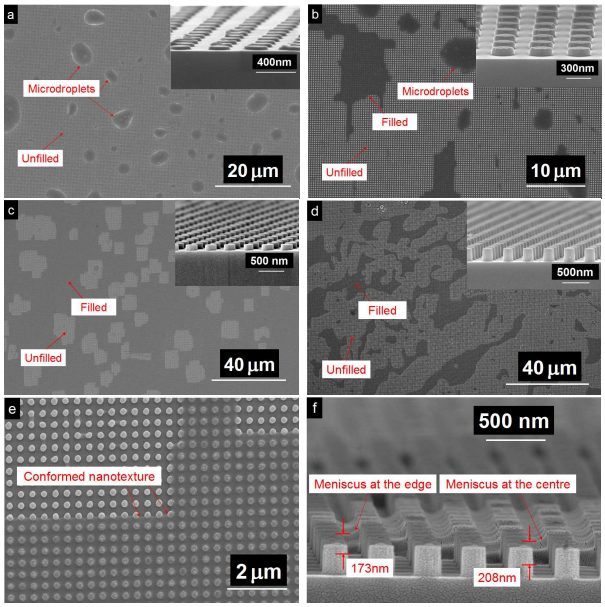

Fig 6. SEM images of HH liquid with 400nm pitch hydrophobic cylindrical nanopost arrays and different post heights: (a) HH liquid on nanopost arrays with height of 35 nm; (b) HH liquid on nanopost arrays with height of 65 nm; (c) HH liquid on nanopost arrays with height of 110 nm; (d) HH liquid on nanopost arrays with height of 250 nm; (e) zoomed-in image of (c); and (f) cross-sectional image HH liquid on nanopost arrays with height of 250 nm.

Conclusions

We developed a novel method for studying wetting behavior of liquid at micro and nano scale via transferring and solidifying UV-curable liquid on nanostructured surface. The solidified samples were applicable to high resolution SEM and AFM measurement. This method was able to extend the nanoscale observation of liquid down to sub-20nm. The wetting behaviors of the liquid were strongly relied on the surface properties and geometries of the nanostructures. The results indicated that macroscopic wetting behavior of liquid is preserved all the way down to 100 nm.

Acknowledgment

This work was jointly supported by the National Nature Science Foundation of China (Grant No. 91023014 and 61306123), the National Basic Research Program of China (973 Program) (Grant No. 2013cb632702), the Priority Academic Program Development of Jiangsu Higher Education Institutions and RFDP and the New Century Excellent Talent Project of the Ministry of Education of China (Grant No. NCET-10-0455).

Notes and references

[a] *Department of Materials Science and Engineering, College of Engineering and Applied Sciences, National Laboratory of Solid State Microstructures, Nanjing University, Nanjing, China.*
E-mail: csyuan@nju.edu.cn

[b] *Department of Mechanical Engineering, University of Hong Kong, Pokfulam, Hong Kong, P. R. C.*
E-mail: liwd@hku.hk

† Electronic Supplementary Information (ESI) available: [SEM images of nanostructures and solidified liquid, AFM images, Contact Angle images of liquid, are presented here]. See DOI: 10.1039/b000000x/

1 R. Wenzel, *Ind. Eng. Chem*, 1936, **28**, 988.
2 A. B. D. Cassie and S. Baxter, *Nature*, 1945, **155**, 21.
3 A. Lafuma and D. Quéré, *Nat. Mater.*, 2003, **2**, 457.
4 Á. Detrich, M. Nyári, E. Volentiru and Z. Hórvölgvi, Mater. Chem. Phys., 2013,**140**, 602
5 S. Jeon, V. Malyarchuk, J. O. White and J. A. Rogers, *Nano Lett.*, 2005, **5**, 1351.
6 Q. Xia, K. J. Morton, R. H. Austin and S. Y. Chou, *Nano Lett.*, 2008, **8**, 3830.
7 P. Kim, H. Y. Kim, J. K. Kim, G. Reiter and K. Y. Suh, *Lab chip.*, 2009, **9**, 3255.
8 D. J. Lee, K. Y. Cho, S. Jang, Y. S. Song and J. R. Youn, *Langmuir*, 2012, **28**, 10488.
9 W. Barthlott, and C. Neinhuis, *Planta.*, 1997, **202**, 1.
10 X. Gao, X. Yan, X. Yao, L. Xu, K. Zhang, J. Zhang, B. Yang and L. Jiang, *Adv. Mater.*, 2007, **19**, 2213.
11 X. Gao and L. Jiang, *Nature*, **2004**,432, 36-36.
12 W. K. Cho, S. Park, S. Jon and I. S. Choi, *Nanotechnology*, 2007, **18**, 395602.
13 S. C. Thickett, C. Neto and A. T. Harris, *Adv. Mater.* 2011, **23**, 3718.
14 K. K. S. Lau, J. Bico, K. B. K. Teo, M. Chowalla, G. A. J. Amaratunga, W. I. Milne, G. H. McKinley and K. K. Gleason, *Nano Lett.*, 2003, **3**, 1701.
15 H. Bai, X. Tian, Y. Zheng, J. Ju, Y. Zhao and L. Jiang, *Adv. Mater.*, 2010, **22**, 5521.
16 S. P. R. Kobaku, A. K. Kota, D. H. Lee, J. M. Mabry and A. Tuteja, *Angew. Chem. Int. Ed.*, 2012, **51**, 10109.
17 J. Z. Wang, Z. H. Zheng, H. W. Li, W. T. S. Huck and H. Sirringhaus, *Nat. Mater.*, 2004, **3**, 171.
18 H. Sirringhaus, T. Kawase, R. H. Friend, T. Shimoda, M. Inbasekaran, W. Wu and E. P. Woo, *Science*, 2000, **290**, 2123.
19 K. F. Lei, *Recent Pat. Nanotechnol.*, 2013, **7**, 81.
20 I Platzman, C. A. Muth, C. Lee-Thedieck, D. Pallarola, R. Atanasova, I. Louban, E. Altrock and J. P. Spatz, *RSC Adv.*, 2013, **3**,13293
21 U. Bauer and W. Federle, *Plant Signal. Behav.*, 2009, **4**, 1019.
22 T. S. Wong, S. H. Kang, S. K. Y. Tang, E. J. Smythe, B. D. Hatton, A. Grinthal and J. Aizenberg, *Nature*, 2011, **477**, 443.
23 P. K. Hansma, G. Schitter, G. E. Fantner and C. Prater, *Science*, 2006, **314**, 601.
24 R. Wang and M. Kido, *Surf. Interface Anal.*, 2005, **37**, 1105.
25 A. Méndez-Vilas, A. B. Jódar-Reyes and M. L. González-Martín, *Small*, 2009, **5**, 1366.
26 D. J. Stokes, *Adv. Eng. Mater.*, 2001, **3**, 126.
27 Y. C. Jung and B. Bhushan, *J. Microsc.*, 2008, **229**, 127.
28 K. Rykaczewski and J. H. J. Scott, *Acs Nano*, 2009, **7**, 5962.
29 R. Seemann, M. Brinkmann, E. J. Kramer, F. F. Lange and R. Lipowsky, *Proc. Natl. Acad. Sci. USA*, 2005,**102**, 1848.
30 T. N. Krupenkin, J. A. Taylor, T. M. Schneider and S. Yang, *Langmuir*, 2004, **20**, 3824.
31 H. Kusumaatmaja, R. J. Vrancken, C. W. M. Bastiaansen and J. M. Yeomans, *Langmuir*, 2008, **24**, 7299.
32 X. Hu, T. Yang, R. Gu, Y. Cui, C. Yuan, H. Ge, W. Wu, W. Li and Y. Chen, *J.Mater.Chem.C*, 2014, **2**, 1836.
33 H. Ge, W. Wu, Z. Li, G. Y. Jung, D. Olynick, Y. Chen, J.A. Liddle, S.Y. Wang and R. S. Williams, *Nano Lett.*, 2005, **5**, 179.
34 Z. Li, Y. Gu, L. Wang, H. Ge, W. Wu, Q. Xia, C. Yuan, Y. Chen, B. Cui and R. S. Williams, *Nano Lett.*, 2009, **9**, 2306.
35 Y. Shen, L. Yao, Z. Li, J. Kou, Y. Cui, J. Bian, C. Yuan, H. Ge, W. Li, W. Wu and Y. Chen, *Nanotechnology.*, 2013, **24**, 465304.
36 D. Quéré, *Annu. Rev. Mater. Res.*, 2008, **38**, 71.
37 J. Bico, C. Tordeux and D. Quéré, *Europhys. Lett.*, 2001, **55**, 214.